Research Square

Preprints are preliminary reports that have not undergone peer review.
They should not be considered conclusive, used to inform clinical practice,
or referenced by the media as validated information.

Experimentally Validated Comparison of Two CFD Simulation Workflows for Oil Jet Cooling and LPTN Improvement

Jon Astier

jastierl@unav.es

Universidad de Navarra

Jon García Urbieta

Dauch Corporation

Hugo Vázquez

Dauch Corporation

Iñigo García

Dauch Corporation

Marco Satrústegui

Centro de Estudios e Investigaciones Técnicas de Gipuzkoa

Ibon Elósegui

Universidad de Navarra

Research Article

Keywords: Automotive applications, electric machine, direct cooling, oil cooling, jet cooling, CFD, HTC, thermal modeling

Posted Date: September 8th, 2026

DOI: https://doi.org/10.21203/rs.3.rs-10537488/v1

License: This work is licensed under a Creative Commons Attribution 4.0 International License.
Read Full License

Additional Declarations: No competing interests reported.

Experimentally Validated Comparison of Two CFD Simulation Workflows for Oil Jet Cooling and LPTN Improvement

Jon Astier[1*], Jon García Urbieta[2], Hugo Vázquez[2], Iñigo García[2], Marco Satrústegui[3], Ibon Elósegui[1]

[1*]Tecnun - Universidad de Navarra, Sede Miramón, Parque Tecnológico de San Sebastián, Paseo Mikeletegi 48, Donostia-San Sebastián, 20009, Spain.

[2]Dauch Corporation (GKN Automotive Zumaia), Street, Zumaia, 20750, Spain.

[3]Grupo de Vehículo Eléctrico, Centro Tecnológico CEIT, Sede Miramón, Parque Tecnológico de San Sebastián, Paseo Mikeletegi 48, Donostia-San Sebastián, 20009, Spain.

*Corresponding author(s). E-mail(s): jastierl@unav.es;
Contributing authors: jon.garcia@gknautomotive.com; hugo.vazquez@gknautomotive.com; inigo.garcia@gknautomotive.com; msatrustegui@ceit.es; ieloseguis@unav.es;

Abstract

The automotive industry is increasingly integrating oil cooling systems in electric motors to address the rising demand for compact, high-performance solutions with efficient thermal management. By directly cooling motor windings and components, oil-based systems provide rapid heat dissipation, enhancing durability, power density, and overall efficiency. This paper presents a comprehensive study on the determination of heat transfer coefficients (HTCs) in hairpin end windings cooled by oil jets. For experimental validation, a functional 3D-printed mockup was designed, allowing for flow observation and precise temperature measurement using PT1000 sensors. Afterwards, two high-fidelity Computational Fluid Dynamics (CFD) simulation approaches are studied: multiphase Finite Volume Method (FVM) and Lagrangian Moving Particle Simulation (MPS). Results demonstrate that both simulation workflows achieve remarkable agreement with experimental data. While the MPS method excels in computational efficiency, the

FVM approach offers a more versatile workflow. Finally, it is demonstrated that integrating these calculated HTCs into Lumped Parameter Thermal Network (LPTN) models drastically improves the accuracy of rapid thermal predictions compared to default correlations. This methodology establishes a robust foundation for the optimization of direct cooling systems in the electric vehicle industry.

Keywords: Automotive applications, electric machine, direct cooling, oil cooling, jet cooling, CFD, HTC, thermal modeling

1 Introduction

The transition to sustainable mobility is driven by the development of electric propulsion systems. At the heart of these powertrains, we find the electric machines, which are demanded to be increasingly compact, efficient, and reliable [1]. Thus, the challenging market requirements directly impact the design of high current density, peak power, and torque density [2]. In this direction, thermal management is a critical aspect of electric machine design, making heat extraction systems the central design limitation [3]. Hence, integrating effective cooling methods becomes a necessity, as well as their design optimization. While standard air cooling cannot provide sufficient heat extraction for high-power density and compact motors [4], liquid cooling solutions present the highest-performing schemes [5]. Water jacket indirect cooling configurations have been a popular choice for the first generations of electric vehicles. However, these approaches have a long conduction path from the main heat sources in the stator winding, especially from the end windings, to the heat sink. Also, this method cannot provide proper cooling for the rotor [4]. Due to these limitations, direct cooling methods have become increasingly popular in the last few years. These schemes allow the extraction of the losses from the main heat generation sources due to the direct contact of a fluid with the components, such as the winding. In these cases, the fluid needs to be non-conducting, leading to the use of a wide range of oils. Some authors proposed the use of oil-submerged semi-flooded cooling solutions, based on the use of a sleeve within the airgap to isolate the rotor and stator [6], [7], [8], [9]. Nevertheless, these designs are rare for automotive commercial products, due to failure risks and potential cooling issues as their main drawback. Therefore, other methods such as spray or jet cooling have been widely studied in many sectors as an efficient heat extraction technology [10]. The simplicity and reliability of jet cooling systems make them ideal for implementation into series-produced commercial products. This technology is most effective when coupled with hairpin windings, due to their superior thermal performance, compared to round wire or other configurations [11], [12]. Besides, another advantage of jet cooling is that it can be well integrated into the powertrain sharing the oil with the transmission and bearing lubrication, optimizing the compactness of the module.

Many authors have experimentally investigated jet cooling configurations applied to the end windings [13], [14], [15], [16], [17]. However, in modern electric machine

design workflows, Computational Fluid Dynamics (CFD) simulations play an essential role in the development of cooling systems, and there is still much space for research in high-fidelity numerical simulation of direct oil cooling systems. Two main simulation approaches have emerged as viable alternatives: Traditional CFD based on the Finite Volume Method (FVM) with multiphase models, and Meshless Lagrangian Moving Particle Simulations (MPS) coupled with thermal models.

The primary advantage of FVM-based CFD lies in its ability to discretize both fluid and solid domains, enabling the simulation of both fluid dynamics and conjugate heat transfer hand in hand. Furthermore, its multiphase modeling capabilities allow the interactions between air and oil to be resolved, obtaining accurate oil distribution, as well as the individual contribution of each phase to heat extraction. Nevertheless, hairpin end windings typically exhibit highly intricate geometries, which lead to very high computational costs for accurate predictions of flow dynamics. Therefore, some authors use simplified geometries that model the end-winding as a toroidal ring [18], [19], while others retain geometric fidelity but limit the model to a small portion of the end-winding region [20].

To the authors' best knowledge, the simulations done by Vanhee et al. in [21], Yang et al. in [22], Yang et al. in [23], and Varghese et al. in [24] represent the best attempts at a faithful FVM-based CFD simulation of an oil dripping system with hairpin winding. Their models include the complete end-winding while maintaining its complex geometry. However, [21] does not present any test-validation and keeps the winding temperature fixed; [22] only compares their model by visually observing similarities in the oil flow pattern and does not heat the winding, nor in simulation, nor in experiments; and [23] addresses these aspects but omits the end-space between the shaft and the end-winding, thereby neglecting oil dripping from the upper to the lower part of the end-winding. [24] addresses all of these issues by combining very high-fidelity separate simulations for the fluid and the solid domains; however, their FVM CFD simulation requires way too many computational resources to run in a feasible time.

By contrast, Meshless Lagrangian MPS offer a significant advantage in terms of computational cost. The absence of mesh results in substantially reduced simulation times compared to FVM-based CFD, making this method particularly attractive to simulate the complete powertrain, including gearbox lubrication and electric motor cooling [25]. However, regarding the end-winding cooling, a key limitation of these approaches is the inability to resolve thermal aspects in solid bodies, and therefore they need to be combined with an additional software in order to resolve conjugate heat transfer [26]. Nevertheless, many authors find good enough agreement between MPS and experimental results [27], [28] [29], [1].

Both of this approaches are oriented towards high-fidelity analysis of fluid flow and conjugate heat transfer, not to fast iterative simulation workflows. In this context, Lumped Parameter Thermal Networks (LPTN) are the preferred approach. These kind of models reduce the motor to a circuit structure that is able to perform very fast thermal assessment; however, their accuracy mainly depends on the thermal resistance and capacitance calculations. Oil jet cooling poses a significant challenge for analytically estimating its thermal resistances; hence, obtaining Heat Transfer Coefficient

(HTC) distributions from a high-fidelity CFD simulation becomes vital for developing an LPTN that accurately predicts the motor's thermal behavior.

In this context, Hefny et al. [19] compare the HTCs obtained from numerical simulations with analytically calculated ones within an LPTN representing the complete motor, highlighting the critical role of accurate HTCs for reliable motor performance prediction. Having a faithful estimation of these would boost the implementation of low computational cost models and, thus, the application of real-time estimation of temperatures in jet oil cooling systems would be enabled [30]. Using digital twins, these models can be calibrated and then embedded onboard in a vehicle [31], resulting in a cluster of virtual sensors during vehicle operation [32].

The objective of this study is twofold. First, to assess and compare two high-fidelity CFD simulation workflows against a dedicated experimental campaign, for which a test bench and a representative mock-up have been built. Second, to extract HTCs from these simulation workflows and incorporate them into a reduced-order LPTN model, whose predictive accuracy is subsequently evaluated against the experimental data.

The paper is arranged as follows: Section 2 describes the oil system and functional mockup used for the experimental campaign. Section 3 introduces the experimental setup and tests performed for the analysis. Section 4 presents the FVM multiphase CFD simulation model and depicts the procedure employed. Section 5 explores the Meshless MPS simulation. Section 6 compares the obtained temperatures from both simulation procedures with the experimental campaign. Section 7 introduces the obtained HTCs in an LPTN and checks for the model accuracy. Finally, Section 8 summarizes the work and presents both conclusions and future work to this research.

2 Description of the System

The oil system to be analyzed was a jet-cooling arrangement that directly impacted the superior surface of the end winding. To validate the proposed cooling method, a 48-slot stator with 4-layer hairpin windings was manufactured and installed in a plastic container designed to accommodate the proposed cooling system, called the "mock-up". This mock-up consisted of a plastic enclosure that supported the stator and encapsulated one side of the end windings, enabling oil cooling in this region, as presented in Fig.1 (left).

This enclosure was 3D printed and designed to accommodate different jet-cooling configurations using an interchangeable part where the oil cooling ducts could be modified.

On the front side of the mock-up, a transparent acrylic glass window was screwed and sealed, to allow the observation of the oil flow while sealing the end winding to avoid oil leakage. This is shown in Fig.1 (left).

Direct current (DC) was applied to the windings as the sole loss source to minimize uncertainties in the mock-up. Since no rotor or alternate current (AC) sources were present, frequency-dependent losses were eliminated. For this purpose, the winding terminals were modified, short-circuiting the phase outputs, as illustrated in Fig.1

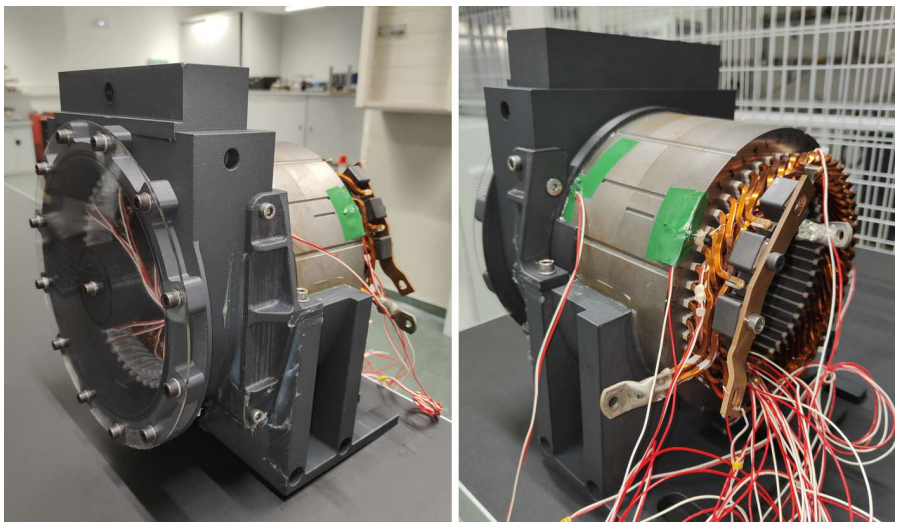


Fig. 1: Mock-up front (left) and rear (right) views.

(right). The neutral point was utilized as the positive pole, while the short-circuited phase outputs served as the negative pole.

3 Experimental Setup and Analysis

This section presents the experimental setup built and the tests conducted for the correlation of the simulation method and the experimental results.

3.1 Experimental Setup

A new test bench was built for the execution of this test. As can be observed in Fig. 2, the described mock-up and stator were fixed on the table. The current was fed by a DC source placed on the right-hand side of the table through a 150 mm^2 cable. The cable was introduced in a current sensor to monitor the current applied to the stator. The PT1000 sensors were plugged into data acquisition hardware to be then retrieved and post-processed. The oil inlet and outlet each had a hose for the input and extraction of the oil into the system. Besides, an oil pump was required to extract all the oil from the stator due to hydraulic head issues.

Most of the mentioned PT1000 sensors were placed in the end winding of interest, the one subjected to the oil cooling. Thus, in the oil-cooled end winding, twelve sensors were located in four positions at 90^{o} and three different layers in each of the positions. The main target was to keep track of the end winding hotspot for correlation studies. Additionally, four sensors were placed in the non-oil-cooled end winding to observe the effect of the system on this side as well. The locations of these sensors in the end winding are depicted in Fig.3. Finally, two more sensors were located in the stator stack and one was employed to measure the ambient temperature.

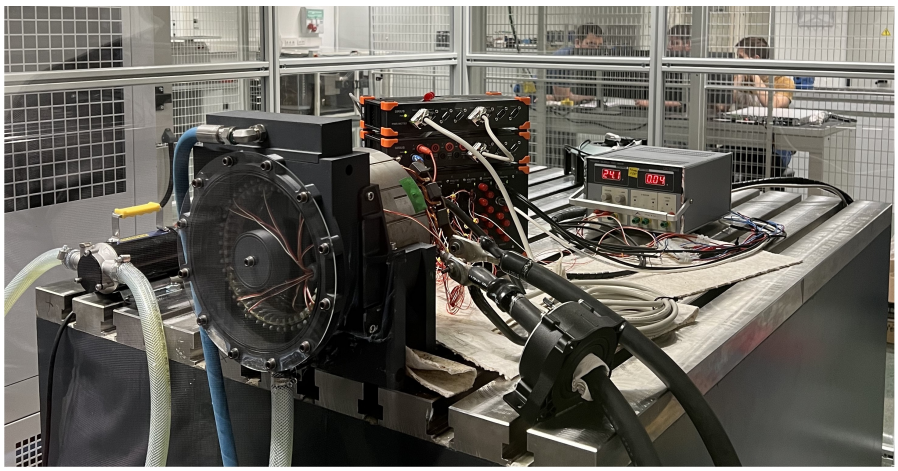


Fig. 2: Experimental setup for the testing campaigns.

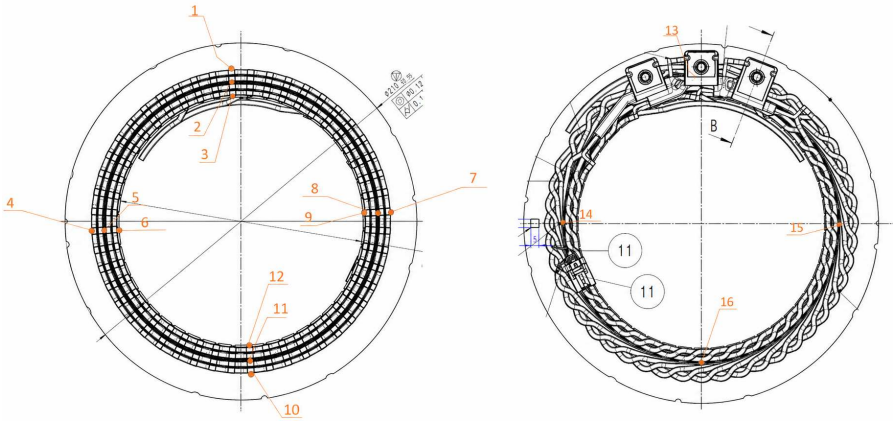


Fig. 3: Location of the PT1000 sensors in the end windings.

3.2 Analysis

Two test campaigns were conducted for this research. The first campaign was carried out without the oil cooling system (chiller, fittings, and coolant sensors) to fine-tune the main power supply, a DC source delivering losses to the stator, and to monitor the stator temperatures.

The second campaign integrated all system components, including the oil cooling system. Various parameters were monitored during this phase using Dewesoft, a commercial data acquisition software. The measurements included system losses (current and voltage at the stator winding terminals), stator temperatures (Fig.3), ambient temperature, and the oil cooling system's key parameters (flow rate and inlet/outlet temperatures of the mock-up).

To characterize the proposed cooling system, four different scenarios were tested with different oil conditions. Two different flow rates, 4 and 8 l/min, and two inlet

temperatures, 40 and 55 ^{o}C, were combined, and the four cases were supplied with DC current of 500 A.

4 Finite Volume Method Multiphase CFD

In this section, a high-fidelity Finite Volume Method CFD methodology was developed in *Ansys Fluent* to characterize the oil-jet cooling configuration. The objective of this model is to capture multiphase dripping behavior, oil distribution across the end winding, and the resulting thermal boundary conditions. Due to the inherently transient nature of dripping and the long thermal time constants involved, the workflow is divided into two stages: (A) transient multiphase dripping simulation, and (B) thermal steady state using the stabilized oil distribution.

4.1 Transient Multiphase Flow Simulation

The first stage models the dripping process using the incompressible transient formulation of the momentum and continuity equations. Solid regions are removed from the fluid solution by marking their cells inactive while preserving mesh integrity. To ensure adequate resolution of oil flow and droplet formation, a mesh with polyhedral cells of approximately 1 mm around the end winding and 3 mm in the surrounding air region is used.

Poubeau et al. proved in [33] and [18] that to correctly capture heat transfer in high-Prandtl-number fluids, it is essential to have at least one cell within the thermal boundary layer. Nevertheless, they also proved the limited impact of the jet impingement area, where the boundary layers are the thinnest, on the total heat transfer over the end-winding area. Therefore, following this criteria that ensures solution accuracy and limits computational cost, inflation layers with a first-cell height of roughly 0.1 mm are applied on the end-winding surface.

A second-order transient formulation is employed with an adaptive time step that ensures an advective Courant number below 20, therefore balancing numerical stability with computational cost. A hybrid Non-Iterative Time Advancement (NITA) scheme is used to reduce the number of outer iterations per timestep, aided by an instability-detection mechanism to maintain robustness.

The dripping regime yields Reynolds numbers in the range of 50-150 for oil and Grashof numbers of order 10^2–10^3 for air. Both values are well below transitional thresholds, so no turbulence model is applied.

The multiphase interaction is modeled using the Volume of Fluid (VOF) method for free-surface flows presented by Hirt and Nichols in [34]. Each computational cell carries an oil volume fraction α, where $\alpha = 1$ represents pure oil, $\alpha = 0$ represents pure air, and $0 < \alpha < 1$ represents interfacial cells. The implicit VOF variant is used because of its superior numerical stability, which enables simulations with bigger timesteps. Gravity is incorporated as a body force, and surface-tension effects are modeled using the Continuum Surface Force (CSF) approach with wall-adhesion modeling.

Material properties are interpolated based on the local oil fraction according to

$$x = \alpha x_{\text{oil}} + (1 - \alpha) x_{\text{air}}, \tag{1}$$

where x denotes any phase-dependent physical property. Fig. 4 shows an oil volume fraction contour over a plane cutting the end-space at the jet central position. It shows clearly the oil flow along the end-winding circumference due to its viscosity, as well as the dripping from the upper to the lower part, and it is used to verify that the oil distribution visually resembles the experimental results.

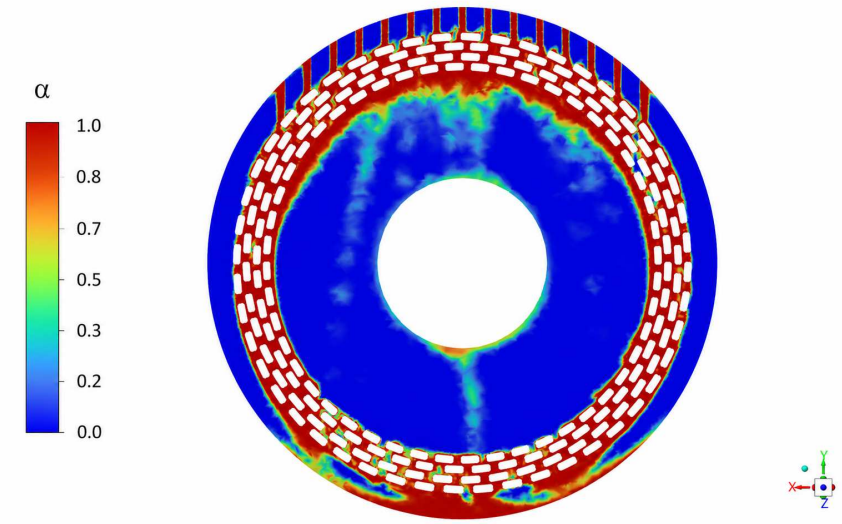


Fig. 4: Oil volume fraction contour at the jet central plane

Both the mean end winding surface oil coverage in different zones and inlet/outlet mass flow rates are monitored until they converge to quasi-steady values. The end winding has been divided in four sections, and Fig. 5 show the stabilization of their oil covered area percentage in the case of 8 l/min and 40 ^{o}C. The oil flow is considered stabilized after 5 seconds.

4.2 Thermal Steady State With Stabilized Oil Distribution

The second stage solves only the energy equation using the oil distribution obtained at the end of the transient simulation. The velocity and pressure fields of Stage 1 are retained to represent convective effects, while the momentum and continuity equations are deactivated to prevent further fluid movement.

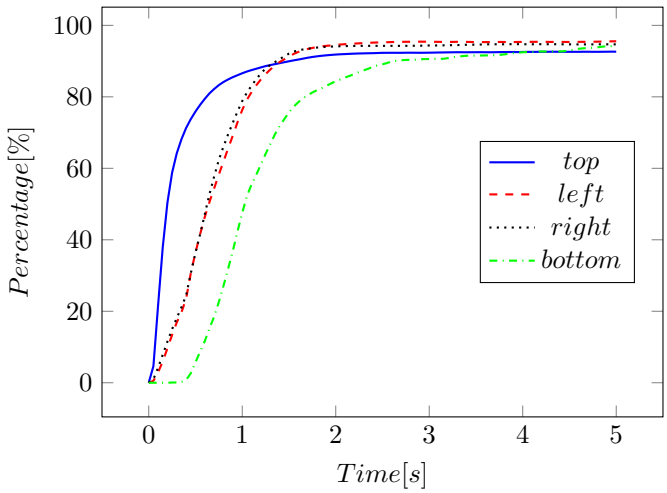


Fig. 5: Mean oil coverage in different zones of the end-winding for 8 l/min and 40 ^{o}C

Volumetric heat generation corresponding to measured winding losses is applied. Convective boundary conditions are applied over the plastic container and the not oil-cooled end winding surfaces to match the experimental natural convection data. Air and oil properties are defined as temperature-dependent piecewise-linear functions.

Accurately modeling the stator and the slot insulation would substantially increase the total cell count in the model. Therefore, for the sake of computational speed, the thermal resistances they pose to the heat path from the winding to the ambient are estimated based on the initial experimental campaign without oil mentioned in section 3. Then, these resistances are added to the active winding's surface.

The enamel coating is also added as a thermal resistance over the whole winding surface. In order to model the insulation varnish over the welded end of the oil-covered end-winding, an additional thermal resistance is added over that surface. Therefore, the slight modifications it can have over the oil distribution are neglected, but most of its thermal effect is retained.

The outcome of this second stage is a fully detailed temperature/heat transfer coefficient map of the winding, like the one seen in Figure 6 for the 8 l/min and 40^{o}C case, enabling the visualization of possible hot spots in the motor. The contour is shown for the entire winding, highlighting the importance of including it completely in the model, even though only one of the end windings is directly cooled.

Both stages have been run in a dedicated server with four 18-core CPUs. Two of them enable multithread calculations, so the Fluent model has been divided into 108 partitions. The first-stage model's mesh consists of 2.9 million cells representing just the fluid part, and for the second stage the solid cells are added, ramping the total cell count up to over 5 million. Taking all of this into account, the first and second stage simulations have taken approximately 142 and 74 hours per case respectively. The second stage's convergence depends on the initialization temperatures, which in this case were already pretty close to the final result because the experimental temperatures were already known.

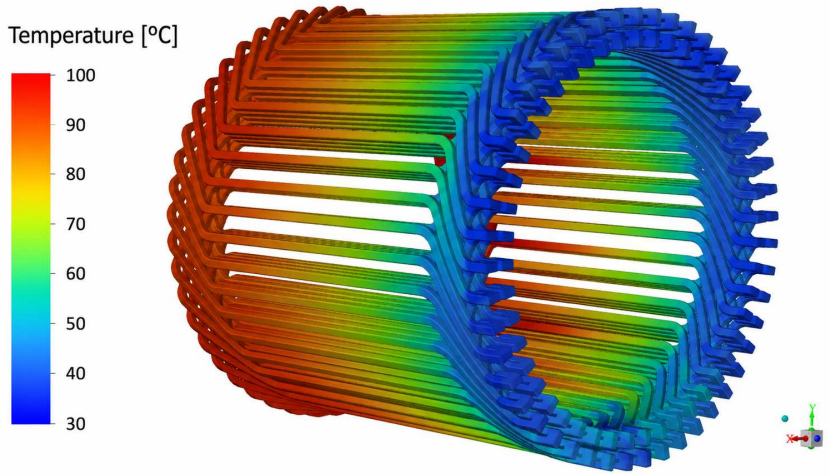


Fig. 6: Temperature contour on the winding

5 Meshless Lagrangian Moving Particle Simulation

This section takes a Lagrangian approach towards fluid dynamics, focusing on the fluid rather than the physical space it takes. Therefore, the fluid is discretized as a set of particles in motion and there's no need for a mesh covering the whole space. This represents a big computational gain in free surface flow, such as jet impingement calculations, when compared to classical Eulerian approaches like the FVM.

The workflow presented in this section has been developed in the commercial software Particleworks, which, among the many Lagrangian CFD approaches in the literature, uses the Moving Particle Simulation (MPS) method presented by Koshizuka and Oka in [35]. This software also incorporates a Finite Element Analysis (FEA) solver for Conjugate Heat Transfer (CHT) simulations.

In the same way as the workflow presented in section 4, the simulation process is divided into two parts: (1) simulating fluid dynamics with the MPS approach, and (2) simulating heat transfer with the FEA solver.

5.1 Moving Particle Simulation

The absence of mesh does not diminish the importance of discretization accuracy, but this time it takes the form of particle size instead of cell size. Setting excessively small particles would drastically increment the computational cost, and going with oversized ones wouldn't capture the flow dynamics as accurately as needed, especially in such intricate geometries as the ones present in hairpin end-windings.

Particleworks includes a feature called "high-resolution regions" that enables the use of different particle sizes for different zones to combine simulation speed with sufficient accuracy in key areas. For this simulation, the area around the end-windings and the nozzles has been defined as high-resolution, and Figure 7 shows the difference

in particle size when dark blue particles reach the end-winding area and become smaller light blue particles.

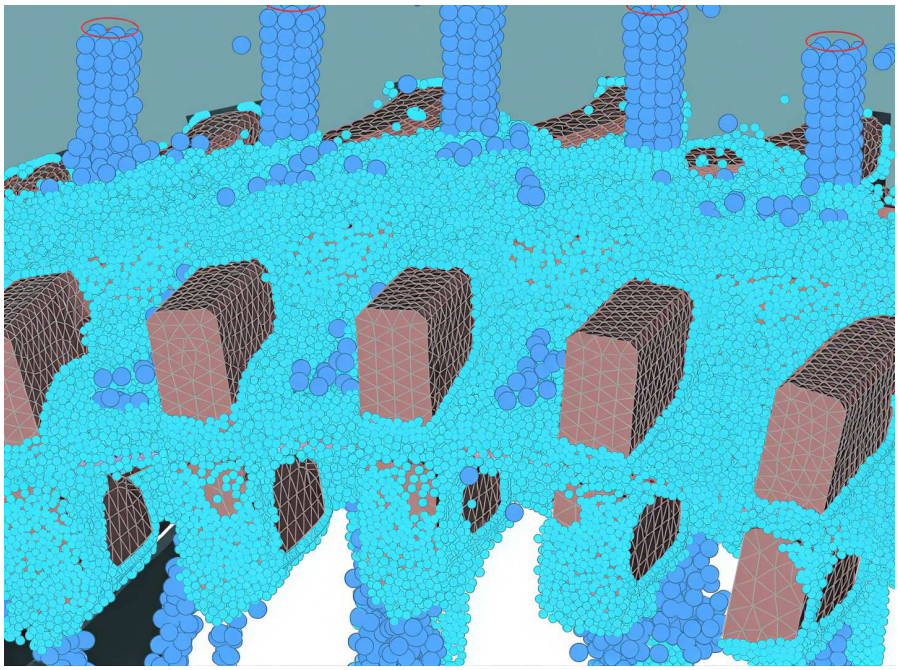


Fig. 7: High fidelity region around the end-winding

To further reduce the number of particles, the manifold region has been isolated and simulated separately. The fluid flow here is considered stationary, and therefore it can be simulated beforehand to determine flow rate and velocity distributions that can be later set as boundary conditions in the main simulation.

Similarly to the previous workflow, the simulation is run for 5 seconds until the oil distribution and velocity-pressure fields are stabilized. Subsequently, the Heat Transfer Coefficients are calculated based on the local Nusselt number correlation. Figure 8 shows an HTC contour over the oil surface, where a similar oil distribution can be observed compared to the one seen in the experimental campaign and in the FVM CFD.

Moving particle simulations are limited to the fluid domain; they are not able to perform any thermal calculation in solids. They need to be complemented with another software iteratively to accurately calculate conjugate heat transfer. The chosen software has been MotorCad due to its low computational cost, and the following workflow has been applied: ParticleWorks is run with an initial end winding temperature estimate; afterwards, the obtained HTC maps are postprocessed, and the average values are fed to MotorCad, which calculates the new temperature to be used in the subsequent ParticleWorks simulation. This process is repeated iteratively until the heat

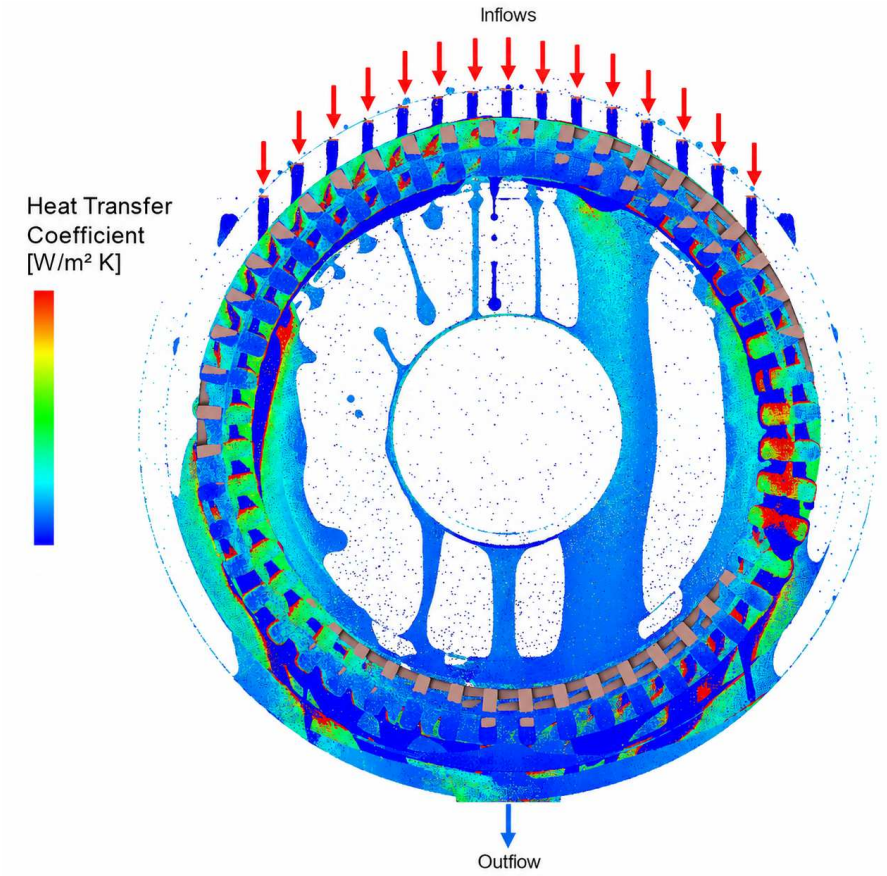


Fig. 8: HTC contour over the oil surface

transfer coefficients stabilize. The better the initial temperature estimation, the lower the number of iterations needed. For greater automation, this whole process, as well as the second stage, a Python-based tool has been developed tailored for this specific case.

5.2 Thermal steady state

In this stage, the thermal Finite Element Analysis (FEA) module available in Particle-Works is used to perform a Steady State analysis. Volumetric heat generation matching the corresponding copper DC losses is applied on the conductors, and importing the HTC maps obtained in the previous stage, the temperature field is resolved.

Similarly to the FVM CFD simulation, a fully detailed temperature map is obtained for the motor's winding, as can be seen in Figure 9. In this case, since this workflow is less computationally expensive than the one presented in section 4, the complete stator has been modeled for a better thermal representation. The developed Python automation tool is prepared to postprocess all of these results and present

clearly key values, like average and maximum temperatures, in different zones of the motor.

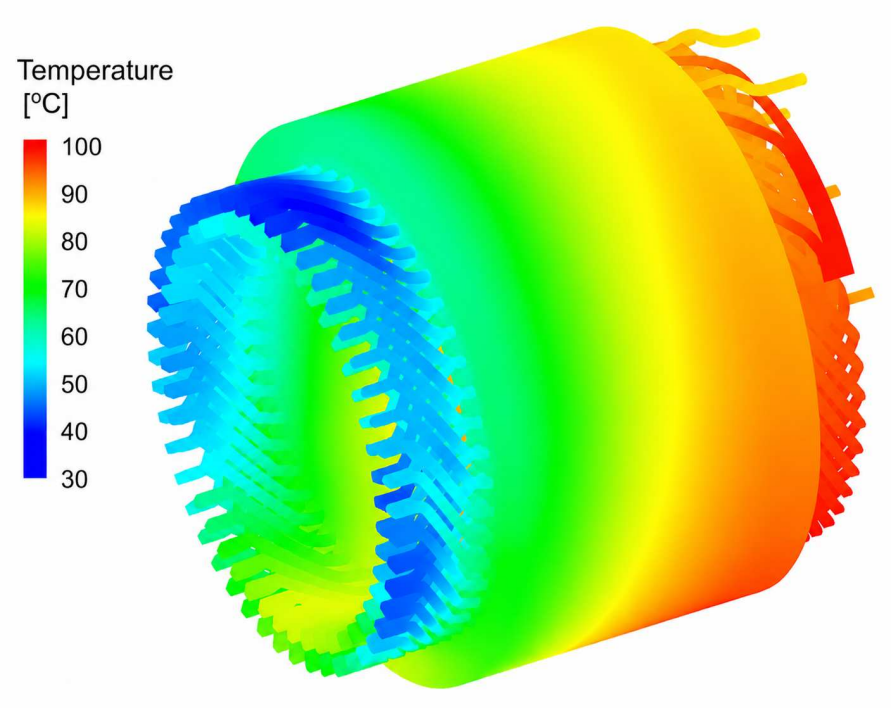


Fig. 9: Temperature contour over the complete motor surface

This complete simulation workflow has been run on a dedicated server with a Tesla V100-PCIE-32GB GPU. The simulation time has been slightly over 6 hours, highlighting both the computational speed of moving particle simulations and the suitability of GPU solvers for CFD simulations.

6 Simulation Results

In this section, in order to validate the workflows depicted in sections 4 and 5, the simulation results are going to be compared against the temperatures measured in the experimental campaign. Tables 1 and 2 present the average and maximum temperatures of the oil side end winding for all the studied cases, while tables 3 and 4 present the same results for the no-oil side. Simulation results are presented as temperature differences (^{o}C) relative to the test results.

The results show an overall good agreement for both simulation workflows. Both workflows are very accurate in the oil side end winding average temperature predictions, but the MPS may not fully capture maximum temperatures, especially at a 4 l/min flow rate. However, MPS seems to be more accurate than the CFD workflow

Table 1: Average temperature results on the oil side end winding

Avg temp [ºC] oil side	**40 ºC inlet**			**55 ºC inlet**		
	Test	**FVM**	**MPS**	**Test**	**FVM**	**MPS**
4 l/min	49.2	+0.3	-2.0	59.3	+1.9	+1.6
8 l/min	46.1	+0.6	-0.1	56.6	-1.7	+3.2

Table 2: Maximum temperature results on the oil side end winding

Max temp [ºC] oil side	**40 ºC inlet**			**55 ºC inlet**		
	Test	**FVM**	**MPS**	**Test**	**FVM**	**MPS**
4 l/min	60.8	+ 2.6	-11.3	72.3	+ 4.2	- 9.3
8 l/min	50.1	+ 0.2	- 2.0	60.4	- 1.6	+ 1.4

Table 3: Average temperature results on the no-oil side end winding

Avg temp [ºC] no-oil side	**40 ºC inlet**			**55 ºC inlet**		
	Test	**FVM**	**MPS**	**Test**	**FVM**	**MPS**
4 l/min	85.5	+ 5.3	- 1.2	95.5	+ 6.9	+ 1.6
8 l/min	83.0	+ 5.3	+ 0.1	92.5	+ 4.0	+ 3.6

in the no-oil side, probably due to the approximation taken in CFD for not modeling the stator iron. All the mean errors for all four cases can be seen in Table 5.

Regarding computational cost, the MPS workflow clearly outperforms the CFD one, and the temperature results' accuracy is similar. Therefore, the MPS looks like the best option for oil jet cooling simulations, but some details should be noted.

The MPS simulation workflow involves iteration between two different softwares, and without an automation tool that can take many workload hours. Building such a tool from scratch requires a big time commitment, but is definitely worth it if it's going to be used extensively over similar electric machines. However, interpreting the HTC maps from ParticleWorks can be complex, and adapting the automation tool to postprocess said maps over very different windings may be challenging. Therefore, for electric machine designers working with many different machines, the CFD workflow may be an overall better option.

In addition, FVM CFD is still run in a CPU solver because some of the used features, like NITA algorithm or enabling simultaneously the multiphase VOF model and the energy equation, are not fully developed yet in Ansys Fluent's GPU solver. In the near future, when all of these options are enabled, this workflow's simulation time may be drastically reduced.

Table 4: Maximum temperature results on the no-oil side end winding

Max temp [ºC] no-oil side	**40 ºC inlet**			**55 ºC inlet**		
	Test	**FVM**	**MPS**	**Test**	**FVM**	**MPS**
4 l/min	86.9	+13.4	- 1.6	96.9	+16.3	+ 1.3
8 l/min	85.0	+ 6.8	- 0.9	94.4	+ 5.6	+ 2.7

Table 5: Mean errors of both simulation workflows

	FVM	**MPS**
Avg temp oil side mean error [%]	2.01	3.18
Max temp oil side mean error [%]	3.31	9.43
Avg temp no-oil side mean error [%]	6.02	1.76
Max temp no-oil side mean error [%]	11.57	1.77

7 Lumped Parameter Thermal Network simulation

As previously stated, one of the main benefits of the thermal simulations presented in sections 4 and 5 is obtaining some HTC values to enhance the accuracy of an LPTN. Hence, this chapter will present the developed model and present the benefits using the HTCs obtained with previous simulation workflows. For this study, the most extended commercially available LPTN will be used, the one in Motor-CAD, and the final temperatures will be compared with the ones obtained using the standard HTC values proposed in the software by default.

To imitate the mock-up presented in section 2 that has been experimentally tested, the Motor-CAD model of the complete motor has undergone a series of modifications. Firstly, oil spray cooling has been applied only to one of the end-windings. In order to emulate the absence of rotor, which is not a native option in this software, both the airgap and the housing node have been changed to be fixed at ambient temperature, and both of their thermal resistances with the stator have been modified to represent heat transfer just by natural convection.

Regarding the Lumped Parameter Thermal Network, the one used in Motor-CAD is a single-slot layout that uses just one tooth and slot to represent the whole stator. Therefore, the HTC values used are an average of all the different conductors, which are manually fed as a stationary HTC, alongside a rotational HTC of zero. In addition, area multipliers have been used to represent the end-winding area covered by oil, which should result in a more accurate thermal resistance calculation.

For the end space modeling, the no-oil side has been set as fully open and the oil side as a closed endcap, both of them with the default correlations proposed. Area multipliers have been used again in both end windings to match the area directly exposed to air. Careful attention has to be paid to this detail since the default option by Motor-CAD is to have both the spray cooling and the endspace area multipliers as one, and therefore calculate both thermal resistances with the total end winding area.

Finally, DC copper losses and ambient temperature have been adjusted to match experimental measurements. As with spray cooling HTCs, natural convection has also been adjusted with values obtained in simulation while the default calculation has been run with Motor-CAD's analytic correlations.

Tables 6 to 9 show the obtained results for average and maximum temperatures in both end windings. Once again, simulation results are presented as temperature differences (ºC) relative to the test results. Case (a) represents the MotorCad run with simulation-fed HTCs, and case (b) is the "by default" MotorCad case.

Table 6: Average temperature results on the oil side end winding

Avg temp [ºC] oil side	**40 ºC inlet**			**55 ºC inlet**		
	Test	**(a)**	**(b)**	**Test**	**(a)**	**(b)**
4 l/min	49.2	- 4.8	+43.7	59.3	- 3.2	+62.1
8 l/min	46.1	- 1.3	+40.3	56.6	- 3.1	+67.6

Table 7: Maximum temperature results on the oil side end winding

Max temp [ºC] oil side	**40 ºC inlet**			**55 ºC inlet**		
	Test	**(a)**	**(b)**	**Test**	**(a)**	**(b)**
4 l/min	60.8	-14.9	+40.6	72.3	-14.7	+60.9
8 l/min	50.1	- 3.9	+45.9	60.4	- 5.4	+43.0

Table 8: Average temperature results on the no-oil side end winding

Avg temp [ºC] no-oil side	**40 ºC inlet**			**55 ºC inlet**		
	Test	**(a)**	**(b)**	**Test**	**(a)**	**(b)**
4 l/min	85.5	+ 1.8	+40.1	95.5	+ 5.8	+73.6
8 l/min	83.0	+ 4.4	+47.6	92.5	+ 5.5	+47.3

These results highlight the substantial accuracy gap between Motor-CAD's default empirical correlations and the physical reality of an oil jet cooling system. Though, to be fair, Motor-CAD clearly states that their model should be calibrated to match

Table 9: Maximum temperature results on the no-oil side end winding

Max temp [ºC] no-oil side	**40 ºC inlet**			**55 ºC inlet**		
	Test	**(a)**	**(b)**	**Test**	**(a)**	**(b)**
4 l/min	86.9	+ 2.3	+40.5	96.9	+ 6.6	+74.8
8 l/min	85.0	+ 4.2	+47.8	94.4	+ 5.7	+47.8

experimental data, adjusting the model to the system-specific characteristics. Anyways, while the standard model drastically overestimates temperatures, the integration of HTCs derived from high-fidelity simulations enables the LPTN model to capture thermal behavior with remarkable accuracy. This qualitative leap in precision transforms the LPTN model from a simple rough estimate into a robust and reliable design tool, facilitating rapid thermal assessments with a degree of confidence that standard commercial tools alone cannot provide.

8 Conclusions and Future Work

This paper has reviewed two different approaches to obtaining high-fidelity HTC through simulation for an oil jet cooling architecture. Initially, an experimental campaign has been carried out over an automotive e-motor with a dedicatedly designed plastic container over the non-drive end winding. Subsequently, two different simulation workflows have been developed: FVM Multiphase CFD and Meshless Lagrangian MPS. Both of them show pretty good agreement with test data, and while FVM offers a more versatile workflow, MPS obtains similar accuracy with a greatly reduced computational cost. Finally, the enhanced accuracy of an LPTN model with externally fed HTCs has been successfully tested.

By integrating advanced simulation tools and iterative workflows, this paper establishes a simulation methodology that enables a comprehensive evaluation of direct oil cooling systems. Future research will focus on applying these workflows to further investigate optimal ways of directly cooling the end winding of electric motors.

9 Statements and Declarations

Funding. This research was funded by the Basque Government through the HAZITEK programme, grant number ZE-2022/00006.

Competing interests. The authors declare that they have no competing interests.

Author contribution. All authors contributed to the study conception and design, material preparation, data collection and analysis. The first draft of the manuscript was written by Jon Astier and all authors commented on previous versions of the manuscript. All authors read and approved the final manuscript

References

[1] Puccio, G. *et al.* Development of direct oil cooling solutions for e-mobility traction motors : Part i: Stator cooling concept. *2023 IEEE International Electric Machines and Drives Conference (IEMDC)* 1–7 (2023).

[2] Shams Ghahfarokhi, P. *et al.* The oil spray cooling system of automotive traction motors: The state of the art. *IEEE Transactions on Transportation Electrification* **9**, 428–451 (2023).

[3] Popescu, M. *et al.* Modern heat extraction systems for power traction machines—a review. *IEEE Transactions on Industry Applications* **52**, 2167–2175 (2016).

[4] Ghahfarokhi, P. S. *et al.* Oil spray cooling with hairpin windings in high-performance electric vehicle motors. *2021 28th International Workshop on Electric Drives: Improving Reliability of Electric Drives (IWED)* 1–5 (2021).

[5] Liu, C. *et al.* Model calibration of oil jet and oil spray cooling in electrical machines with hairpin windings. *2021 IEEE Energy Conversion Congress and Exposition (ECCE)* 3813–3820 (2021).

[6] Ismagilov, F. R., Vavilov, V. Y., Bekuzin, V. I., Ayguzina, V. V. & Permin, D. Y. Analysis of stator cooling methods of fault-tolerant electric machines. *2020 Fifteenth International Conference on Ecological Vehicles and Renewable Energies (EVER)* 1–6 (2020).

[7] Acquaviva, A., Skoog, S. & Thiringer, T. Design and verification of in-slot oil-cooled tooth coil winding pm machine for traction application. *IEEE Transactions on Industrial Electronics* **68**, 3719–3727 (2021).

[8] Rocca, A. L. *et al.* Thermal management of a high speed permanent magnet machine for an aeroengine. *2016 XXII International Conference on Electrical Machines (ICEM)* 2732–2737 (2016).

[9] Paredes, J. *et al.* New oil-flooded direct stator cooling system for high power density machines with hairpin windings. *IEEE Access* **14**, 9838–9850 (2026).

[10] Jambunathan, K., Lai, E., Moss, M. & Button, B. A review of heat transfer data for single circular jet impingement. *International Journal of Heat and Fluid Flow* **13**, 106–115 (1992). URL https://www.sciencedirect.com/science/article/pii/0142727X92900174.

[11] Taniguchi, M. *et al.* Development of new hybrid transaxle for compact-class vehicles (2016). URL https://api.semanticscholar.org/CorpusID:111827383.

[12] Nobuyasu, S. *et al.* Development of new hybrid transaxle for mid-size sports utility vehicles (2020).

[13] Davin, T., Pellé, J., Harmand, S. & Yu, R. Experimental study of oil cooling systems for electric motors. *Applied Thermal Engineering* **75**, 1–13 (2015).

[14] Kekelia, B. *et al.* Surface temperature effect on convective heat transfer coefficients for jet impingement cooling of electric machines with automatic transmission fluid. *ASME 2019 International Technical Conference and Exhibition on Packaging and Integration of Electronic and Photonic Microsystems (IPACK2019)* (2019).

[15] Liu, C. *et al.* Experimental investigation of oil jet cooling in electrical machines with hairpin windings. *IEEE Transactions on Transportation Electrification* **9**, 598–608 (2023).

[16] Chen, P., Ben Hassine, N., Ouenzerfi, S. & Harmand, S. Experimental and numerical study of stator end-winding cooling with impinging oil jet. *Applied Thermal Engineering* **220** (2023).

[17] Ha, T., Han, N. G., Kim, M. S., Rho, K. H. & Kim, D. K. Experimental study on behavior of coolants, particularly the oil-cooling method, in electric vehicle motors using hairpin winding. *Energies* **14** (2021). URL https://www.mdpi.com/1996-1073/14/4/956.

[18] Poubeau, A., Vinay, G., Mendes Alves, B., Bai, X. & Viot, P. Numerical simulations of direct liquid cooling of the end-windings of an electric machine. *International Journal of Heat and Mass Transfer* **235** (2024).

[19] Hefny, H., Z. Haddad, R., Al-Ani, D., Emadi, A. & Bilgin, B. Numerical multiphase thermal analysis to determine end-winding heat transfer coefficient of an interior permanent magnet motor. *2025 IEEE/AIAA Transportation Electrification Conference and Electric Aircraft Technologies Symposium (ITEC+EATS)* (2025).

[20] Maddumage, W., Ouenzerfi, S., Harmand, S. & Cairns, A. Thermal management of hairpin winding traction motors in electric vehicles: Parametric evaluation of impinging oil jet cooling using cfd simulations. *Applied Thermal Engineering* **273** (2025).

[21] Vanhee, S., Pawar, J., Desmet, F., Nonneman, J. & De Paepe, M. Thermal analysis of an oil jet cooled electric motor with hairpin windings. *2024 International Conference on Electrical Machines (ICEM)* (2024).

[22] Yang, C., Cai, W., Xie, Y. & Shao, B. Experiment and simulation study on the cooling performance of oil-cooling pmsm with hairpin winding. *Machines* **12** (2024).

[23] Yang, H. *et al.* Study of the thermal performance of oil-cooled electric motor with different oil-jet ring configurations. *Energies* **18** (2025).

[24] Varghese, J., Schlautman, J., Chen, Y., Bhunia, S. & Srinivasan, C. 3d cht simulation of oil-cooled electric motors: A comparative study of standard and paperless design. *SAE Technical Paper* (2025).

[25] Han, N. G. *et al.* Thermal analysis of the oil cooling motor according to the churning phenomenon. *Applied Thermal Engineering* **220** (2023).

[26] Merelli, M. e-motor cooling with oil jets: impact of flowrates and oil properties. *2023 AEIT International Conference on Electrical and Electronic Technologies for Automotive (AEIT AUTOMOTIVE)* (2023).

[27] Gai, Y., Soulard, J., Ma, X. & McMahon, R. Numerical and experimental investigation of fluid flow and heat transfer in hairpin end-winding for an oil-injected cooled traction motor. *IEEE Transactions on Transportation Electrification* **11**, 7243–7251 (2025).

[28] Ha, T. & Kim, D. Study of injection method for maximizing oil-cooling performance of electric vehicle motor with hairpin winding. *Energies* **14**, 747 (2021).

[29] Beom, T. *et al.* Development of a coefficient of performance to evaluate the oil cooling methods in electric vehicle motors. *Case Studies in Thermal Engineering* **71** (2025).

[30] García Urbieta, J. *et al.* Sensitivity analysis of lumped-parameter thermal networks for the experimental calibration of emotor models. *IEEE Transactions on Transportation Electrification* **10**, 6210–6220 (2024).

[31] Urbieta, J. G. *et al.* Efficient calibration of lptn models for digital twins of epowertrain motors. *2023 13th International Electric Drives Production Conference (EDPC)* 1–8 (2023).

[32] Urbieta, J. G. *et al.* Consideration of thermal ageing in digital twins of automotive-grade electric motors. *2024 International Conference on Electrical Machines (ICEM)* 1–7 (2024).

[33] Poubeau, A., Vinay, G., Kekelia, B. & Bennion, K. Numerical simulations of high prandtl number liquid jets impinging on a flat plate. *International Journal of Heat and Mass Transfer* **205** (2023).

[34] Hirt, C. W. & Nichols, B. D. Volume of fluid (vof) method for the dynamics of free boundaries. *Journal of Computational Physics* **39**, 201–225 (1981).

[35] Koshizuka, S. & Oka, Y. Moving-particle semi-implicit method for fragmentation of incompressible fluid. *Nuclear Science and Engineering* **123**, 421–434 (1996).